RSC Advances

PAPER

View Article Online
View Journal | View Issue

Cite this: *RSC Adv.*, 2022, **12**, 30514

Large-scale synthesis of mixed valence $K_3[Fe_2S_4]$ with high dielectric and ferrimagnetic characteristics†

Mohammad R. Ghazanfari, [a] Archa Santhosh, [b] Johannes C. Vrijmoed, [c] Konrad Siemensmeyer, [d] Bertram Peters, [e] Stefanie Dehnen, [e] Paul Jerabek [b] and Günther Thiele *[a]

High yields of phase-pure $K_3[Fe_2S_4]$ are obtained using a fast, straight-forward, and efficient synthetic technique starting from the binary precursors K_2S and FeS, and elemental sulphur. The compound indicates soft ferrimagnetic characteristics with magnetization of 15.23 A m^2 kg^{-1} at 300 K due to the mixed valence of Fe^{II}/Fe^{III}. Sintering at different temperatures allows the manipulation of the microstructure as well as the ratio of grains to grain boundaries. This results in a variation of dielectric and impedance properties. Samples sintered at 923 K demonstrate a dielectric constant (κ) of around 1750 at 1 kHz, which lies within the range of well-known high-κ dielectric materials, and an ionic conductivity of 4×10^{-2} mS cm^{-1} at room temperature. The compound has an optical band gap of around 2.0 eV, in agreement with tailored quantum chemical calculations. These results highlight its potential as a material comprising non-toxic and abundant elements for electronic and magnetic applications.

Received 19th August 2022
Accepted 13th October 2022

DOI: 10.1039/d2ra05200h

rsc.li/rsc-advances

Introduction

The growing implementation of microelectronic technology in day-to-day life applications results in an increasing demand for quantum materials with novel properties and high performances, with a recent focus on spintronic applications.[1] Spintronic materials are commonly designed as multi-layer "sandwich" composites of magnetic or non-magnetic films with the degree of freedom of the electron spin having an important role in the materials' performance.[2] Distinctly, a higher spin polarisation leads to an increased performance in the applications, such as faster data processing, lower energy consumption, and higher circuit density.[2] Some ferromagnetic and ferrimagnetic materials can potentially display 100% spin polarisation near the Fermi energy level, indicating an outstanding performance for spintronics.[3]

The correlation of electronic and magnetic characteristics of materials is a crucial point for spintronic applications. Ferromagnetic and ferrimagnetic materials such as Heusler alloys,[4] zinc blende compounds,[5,6] and magnetic ceramics[7,8] provide a combination of both electronic and magnetic properties, introducing ideal candidates for the spintronic applications.[3,8,9]

Beside the electronic and magnetic behaviours, the impact of resource mining on the environment, as well as the production costs are further challenging aspects in the development of new materials.[10] In recent years, the design and synthesis of quantum materials consisting of environmentally and ecologically friendly components has attracted considerable attention in different fields of chemistry, physics, and materials engineering. To tailor and improve the electronic, dielectric, and magnetic properties of materials, different approaches such as manipulation of microstructures, hybridization of compounds, and doping of modifier additives are introduced.[11–13] Due to abundant resources of sulphur and iron, ternary sulphido ferrate compounds, comprising $[Fe_xS_y]^{q-}$-anionic or -polyanionic substructures, are one of the most promising cost-effective and non-toxic materials for potential applications such as semiconductors, superconductors, sensors, and magnetic storage devices.[14,15] Iron-based chalcogenide families are the most available and practical compounds with straightforwardly adjustable electronic and magnetic characteristics.[16,17]

[a]Fachbereich Biologie, Chemie, Pharmazie, Freie Universität Berlin, Fabeckstr. 34-36, 14195 Berlin, Germany. E-mail: guenther.thiele@fu-berlin.de
[b]Institute of Hydrogen Technology, Helmholtz-Zentrum Hereon, Max-Planck Straße 1, 21502 Geesthacht, Germany
[c]Fachbereich Geowissenschaften, Freie Universität Berlin, Malteserstr. 74-100, 12249 Berlin, Germany
[d]Helmholtz-Zentrum Berlin für Materialien und Energie, Hahn-Meitner-Platz 1, 14109 Berlin, Germany
[e]Fachbereich Chemie, Philips-Universität Marburg, Hans-Meerwein-Straße 4, 35032 Marburg, Germany

† Electronic supplementary information (ESI) available. CCDC 2195992. For ESI and crystallographic data in CIF or other electronic format see DOI: https://doi.org/10.1039/d2ra05200h

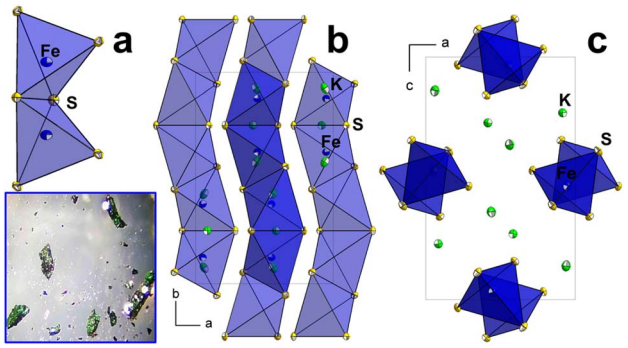

Fig. 1 Representation of the crystal structure of **1**. (a) Edge-sharing $[Fe^{II/III}S_4]^{n-}$-tetrahedra. (b) and (c) Zigzag chain of anionic substructures depicted in [001] and [010], respectively. (Inset) Optical microscopy photograph of the obtained single crystals of **1** covered by Paratone® oil at 80× magnification. Selected bond lengths (Å) and angles (°): Fe–S = 2.2770(12)–2.3404(12), K–S = 3.0876(17)–3.3571(14), and S–Fe–S = 100.47(8)–111.11(9) at 100 K, and Fe–S = 2.282(3)–2.346(3), K–S = 3.105(5)–4.491(4), and S–Fe–S = 100.25(10)–115.08(12) at room temperature.

All literature reported alkali metal sulphido ferrates with one-dimensional anionic sublattices, such as $A[FeS_2]$[18] and $A[Fe_2S_3]$[19] (A = Na, K, Cs), $A_8[Fe_4S_{10}]$ (A = Rb, Cs),[20] $Na_2[FeS_2]$,[21] $Na_7[Fe_2S_6]$,[21] and $K_7[Fe_5S_{10}]$[22] comprise connected $[FeS_4]$-polyhedra with resulting substructures of a linear chain. However, $K_3[Fe_2S_4]$ (**1**),[23] and its isotypic homologues $Na_3[Fe_2S_4]$,[24] $Rb_3[Fe_2S_4]$,[23] $Cs_3[Fe_2S_4]$,[23] $Na_3[Fe_2Se_4]$,[25] $K_3[Fe_2Se_4]$,[26] and $Cs_3[Fe_2Se_4]$[27] exhibit a zigzag-arrangement of edged-shared $[FeS_{4/2}]$-tetrahedra (Fig. 1). The resulting chain sub-structures contain mixed-valence Fe in the oxidation state of II and III. As the main driving force to investigate $K_3[Fe_2S_4]$, the zigzag motif of anionic sublattice in addition to the presence of mixed-valence iron ions could synergically provide stronger interatomic interactions and possibly improve the magnetic and electronic properties. This series of compounds crystallise in the orthorhombic space group *Pnma* with four molecular units per unit cell.

The original synthesis of **1** was reported by Bronger *et al.* in 1994, heating potassium carbonate, elemental sulphur and iron, to 930 K for 20 hours in a continuous flow of hydrogen.[23] The yield, purity, and side products of the synthesis are not reported, although the formation of alkali metal sulphates, hydroxides, and polysulphides as side products would be expected due to the use of an excess of potassium carbonate and sulphur in the initial stoichiometry. The formation of water according to the reaction equation in Scheme 1, suggests at least a partial formation of iron oxides and hydroxides. To the best of our knowledge, no characterisation of **1** beyond the structural description, nor a synthetic approach for phase-pure material has been reported yet.

$$3\,A_2CO_3 + 8\,S + 4\,Fe + 3\,H_2 \xrightarrow[\approx 20\ h]{930\ K} 2\,A_3[Fe_2S_4] + 3\,CO_2 + 3\,H_2O$$

Scheme 1 Idealized reaction equation of the reported synthesis of **1**. Alkali metal carbonate and sulphur were used in two- to three-fold excess which are not considered in the equation.

Herein, we describe the hitherto unreported electrical, optical, and magnetic properties of **1**, including a straightforward synthesis to yield multi-gram batches of phase-pure **1**.

Result and discussion

Synthesis and structural characterisation

Intimate mixture of stoichiometric amounts of K_2S, FeS, and elemental sulphur in a silica glass ampoule is heated to approx. 1200 K for five minutes to yield pure **1** without further purification necessary. The yield is quantitative with up to 50 g isolated per batch, only limited by the size of the ampoule. The product is a dark green powder with a metallic shimmer. Powder of **1** is sensitive to air and moisture and needs to be handled under inert atmosphere. Single crystals of **1** were obtained as metallic green plates by solvothermal treatment of the crude product in ethylenediamine at 423 K for 48 hours. In accordance with the literature, the crystallographic refinement confirms the space group *Pnma*.[23] The lower measurement temperature of 100 K in this work, results in the slightly shortened unit-cell parameters and bond lengths compared to the measurement temperature of 295 K, which was used in 1994 (in brackets): a = 7.1219(4) Å (7.157(3) Å), b = 10.9301(6) Å (10.989(4) Å), c = 11.4840(7) Å (11.560(4) Å), V = 893.95(9) Å^3

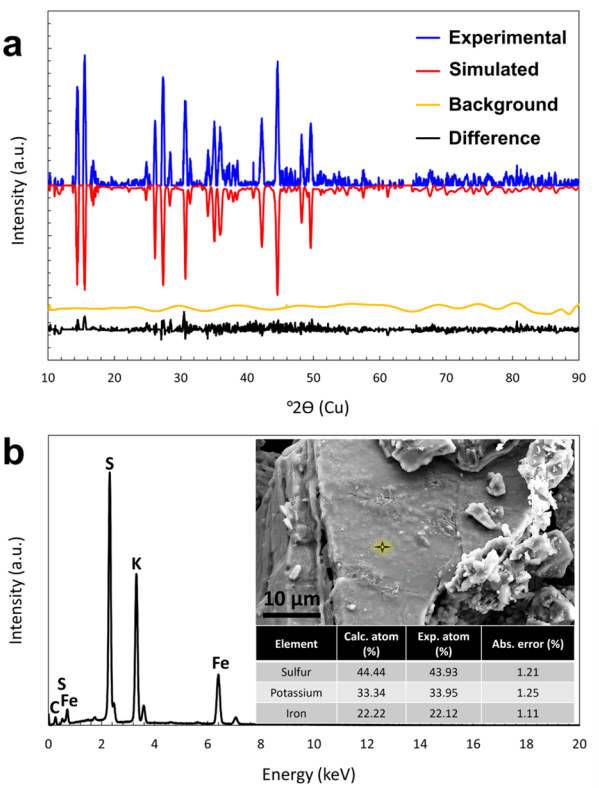

Fig. 2 (a) Powder X-ray diffraction (PXRD) diffractogram (blue) compared to the Rietveld simulated pattern (red). (b) EDX spectrum of **1**. High resolution backscattered electron image obtained with a field emission scanning electron microscope (FE-SEM) with beam energy of 20 kV.

(909.17 Å^3). Full details on the structure solution and refinement are available in the ESI.†

Rietveld refinement of the powder X-ray data (Fig. 2a) ascertains the phase-purity of the compound with a degree of crystallinity of 96.5% ± 2% and an average crystallite size of 465 nm ± 3%. The list of main detected reflections in PXRD analysis (conducted at room temperature) as well as indexes of corresponding crystal planes are provided in the ESI, Table S4.† The chemical composition and homogeneity were confirmed by energy dispersive X-ray spectroscopy (EDX) coupled with scanning electron microscopy (SEM) measurements (Fig. 2b). The obtained chemical stoichiometry based on EDX results is $K_{3.09}[Fe_{2.01}S_4]$ which is comparable to the ideal stoichiometry of 3 : 2 : 4.

The infrared spectrum of **1** indicates four weak absorption bands in the wavenumber range of 1015 to 460 cm^{-1} (see the ESI†). The absorption bands of Fe–S are expected at wavenumbers lower than 400 cm^{-1} and do not lie within the measurement range.[28]

The thermal behaviour of **1** was investigated using differential scanning calorimetry (DSC) coupled with a thermogravimetric analysis (TG). The TG profile (Fig. S1†) displays a negligible mass loss of 0.27% upon heating to 1023 K, indicating the mass stability of **1**. Endothermic and exothermic events at around 950 K in the heating and cooling scans, respectively, can be attributed to the melting point.

Magnetic properties

In **1**, due to charge compensation considerations, assuming common oxidation states of potassium (+1) and sulphur (−2), the formal oxidation state of iron will be +2.5 which would suggest a mixed-valent combination of +2 and +3. Crystallographically, those are undistinguishable since they tend to occupy equal positions in the structure. However, the magnetic studies on the isotypic structures of $Na_3[Fe_2S_4]$ and $Na_3[Fe_2Se_4]$,[29] suggest the co-existence of Fe^{II} and Fe^{III}. Due to the mixed-valence nature of the iron ions in **1**, magnetic properties were investigated based on the field-dependent magnetisation curves at the temperatures of 3 and 300 K.

According to the trend of the magnetisation curve as a function of the applied field (Fig. 3a), both curves indicate narrow hysteresis loops with coercivity values of around 2 mT and 3 mT, as well as remanence values of around 0.1 and 0.3 A m^2 kg^{-1}, at 3 and 300 K, respectively. The relatively low values of coercivity and remanence can be considered as a sign of soft ferrimagnetic behaviour of the material. However, these values are higher those obtained for other potassium sulfido ferrates (II or III).[19,30] Such an increased magnetisation can be explained by the co-existence of Fe^{II} and Fe^{III} ions and the resulting exchange mechanisms. Direct exchange and superexchange can create the magnetic domains with a coercivity and a remanence. Both mechanisms rely on a suitable distance between the magnetic ions. According to a Fe–Fe distance of 2.78(19) Å along the [FeS]-chains in **1**, a direct exchange can be considered as the main magnetic interaction.[31] This mixed-valence situation is supported by the ferrimagnetic ordering observed in **1**.

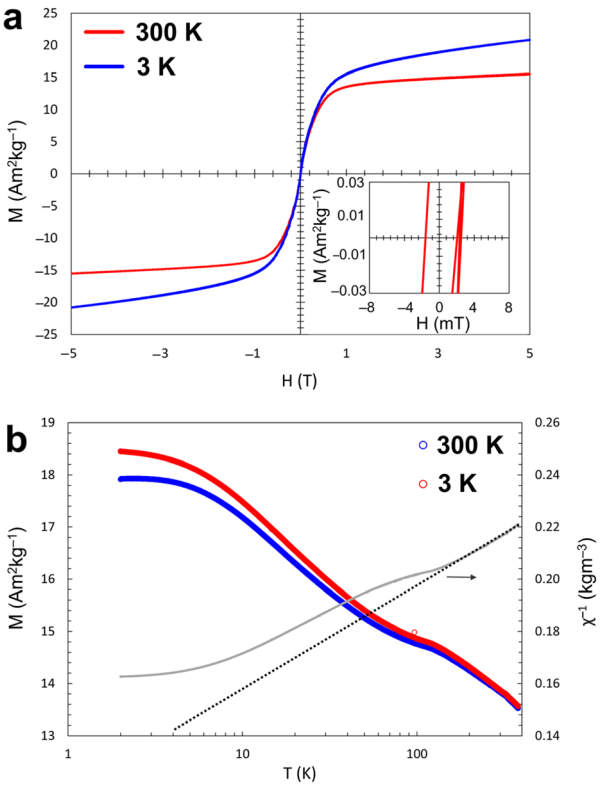

Fig. 3 (a) Field-dependent magnetisation hysteresis curves at different temperatures using applied fields of up to 5.00 T. (Inset) Close-up view of the curve at 300 K. (b) Temperature-dependent magnetisation curves. FC (blue) and ZFC (red) curves under an applied field of 5 mT. Right axis: FC (grey) curve of χ^{-1} variations as a function of temperature under an applied field of 5 mT. Black dotted lines: fitting lines with the Curie–Weiss law.

The magnetisation value of **1** (15.23 A m^2 kg^{-1} at 300 K) lies in the range of 3d transition metal ferrites with inverse-spinel crystal structures, such as $CoFe_2O_4$ (41 A m^2 kg^{-1}),[32] $NiFe_2O_4$ (19.97 A m^2 kg^{-1}),[33] and $MnFe_2O_4$ (17.4 A m^2 kg^{-1}),[34] as the well-known ferrimagnetic compounds, although the magnetization mechanism could be significantly different due to the dissimilarities in the crystal structure and coordination chemistry.

Materials with such a magnetisation value are frequently employed in numerous magnetic-based applications such as energy storage technologies,[35] water treatment,[36] catalysts,[37] and biomedical therapeutic applications.[38]

The temperature-dependent magnetic measurements of zero field cooled (ZFC) and field cooled (FC) were performed under an applied field of 0.5 T, indicating the decrease in magnetisation as a function of increasing temperature (Fig. 3b). The separated curves of FC and ZFC with the irreversible bifurcation temperature of around 320 K indicate an internal magnetic disorder, which could be caused by tiny amount of phase impurity (non-detectable by XRD), crystal defect, or geometrical magnetic frustration.[39] Crystal defects such as vacancies can create a localized magnetically disordered area within the structures and introduce a deviation from ideal ferrimagnetic ordering. In addition, geometrical magnetic frustration can occur in special geometrical motifs with odd numbers of

magnetic moments, for example, in the vicinity of vacancies or near to the surface of the material.[39]

Magnetometry results depict the soft ferrimagnetic characteristic of **1**, which is in agreement with the reported behaviour for the isotypic structures of $Na_3[Fe_2S_4]$ and $Na_3[Fe_2Se_4]$.[29] However, there is no report on the quantity of magnetization for these compounds.

The ferrimagnetic properties of **1** can be assumed to arise from the antiparallel alignment of two magnetic sublattices including the Fe^{II} and Fe^{III} ions with different magnitudes of the magnetic moments. In addition, the curve of the inverse magnetic susceptibility as a function of temperature (Fig. 3b), confirms the antiferromagnetic ordering of **1** by a significant deviation from the fitted line of the Curie–Weiss law for paramagnetic behaviour.[40]

Microstructural and electrical properties

Regarding the significant impact of the microstructure of the solid on its electrical properties, the microstructures of the prepared bulk samples were studied using field emission scanning electron microscopy technique (FE-SEM). SEM micrographs of sintered pellets (Fig. 4) indicate relative uniformity of the grains in size and shape with an average grain size of around 8, 23, and 52 μm for samples sintered for 15 hours at 723, 823, and 923 K, respectively.

Increasing the sintering temperature leads to an increase of the grain size and decreases the ratio of grain boundaries to grains. The accessible sintering temperature of **1** is limited by the compound's melting point, which was determined to be around 950 K.

Strong dependency of the electronic and transferring properties to the crystal structure led us to perform impedance and dielectric measurements of **1**.

In the frequency range of 0.10 to 10 kHz, the dielectric constants for all samples rapidly decrease from 3200 to 150, 3400 to 420, and 5450 to 550 for samples sintered at 723, 823, and 923 K, respectively. The diminishing of the space charge polarisation mechanism, one of the active electrical polarisation mechanisms at low frequencies, is considered the main reason for this trend, while the rest of the polarisation mechanisms including dipolar relaxation as well as ionic and electronic resonances are still active in the frequency range of the measurements.[39] The dielectric constant of **1** when sintered at 923 K was found to be 1750 at the frequency of 1 kHz and ambient temperature, which were chosen as the standard conditions for the dielectric measurements. The obtained value is orders of magnitude larger compared to the reference material SiO_2 ($\kappa = 3.9$) as the insulator materials for the MOSFET gates,[41] and even significantly higher than some of the commercial high-κ dielectric materials such as barium and strontium titanates for the circuit capacitor applications.[42]

At high frequencies in the range of 15 to 100 kHz, dielectric constant values are obtained in the range of 150 to 100, 420 to 350, and 550 to 450 for samples sintered at 723, 823, and 923 K, respectively. In a similar trend, the dielectric loss values of all pellets are high for small frequencies and sharply decrease to a plateau for high frequencies (Fig. 5a). In the frequency range of 0.40 to 100 kHz, the loss values vary from 1.26 to 0.04, 1.04 to 0.03, and 0.97 to 0.01 for samples sintered at 723, 823, and 923 K, respectively. At frequencies lower than 0.40 kHz, the dielectric loss measurements were too noisy to allow for a reliable evaluation.

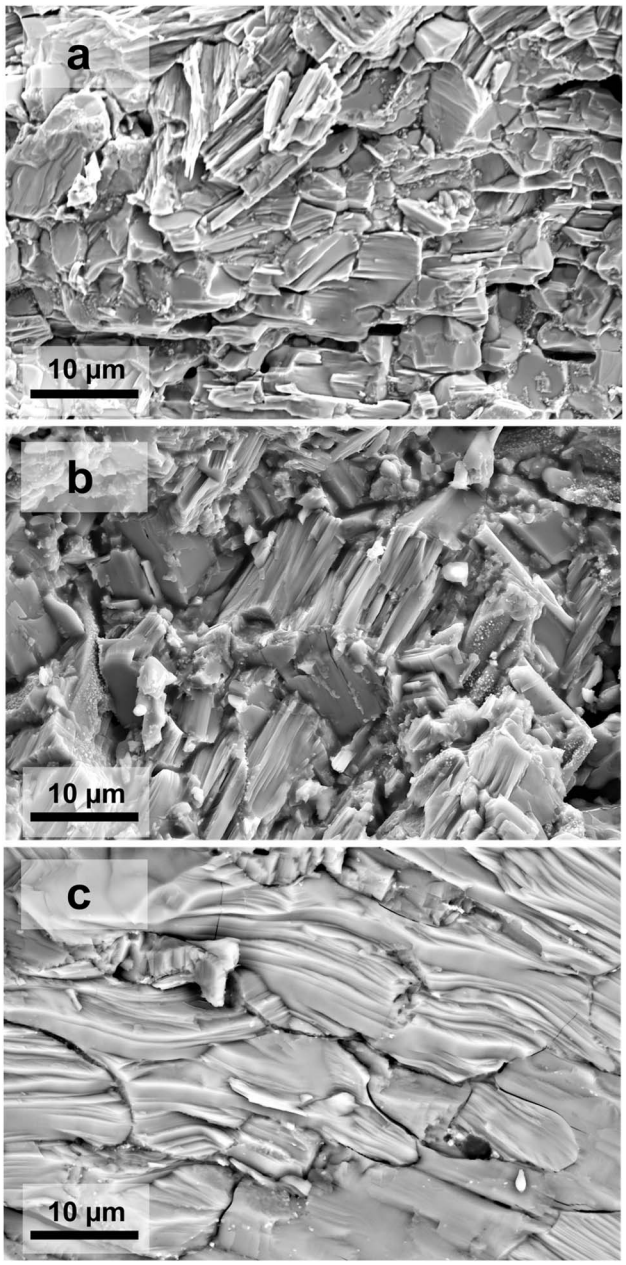

Fig. 4 FE-SEM high resolution secondary electron image with beam energy of 20 kV from the cross section of pellets of **1** sintered at different temperatures. (a) Pellet sintered at 723 K, (b) Pellet sintered at 823 K, (c) Pellet sintered at 923 K.

Comparing the dielectric results of the samples sintered at different temperatures, it becomes clear that a higher dielectric constant and a lower dielectric loss is obtained for the pellet sintered at the highest temperature, *i.e.*, 923 K. Because of the close dependency of the dielectric properties to the bulk density

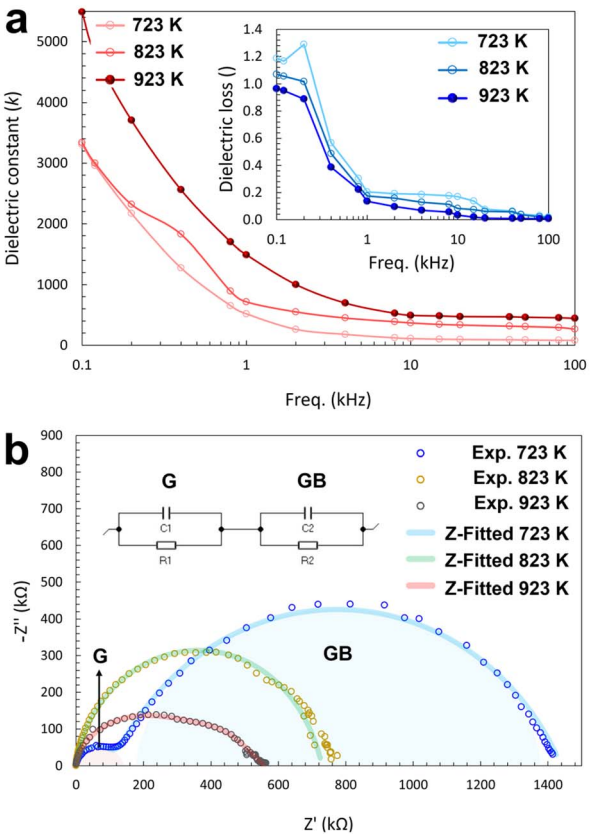

Fig. 5 (a) Dielectric constant variations of pellets of **1** sintered at different temperatures as a function of the frequency in the range of 0.10 to 100 kHz. (Inset) Dielectric loss variations of the sintered pellets at different temperatures as a function of the frequency in the range of 0.10 to 100 kHz. (b) Nyquist plot of pellets of **1** sintered at different temperatures (dotted lines), as well as fitted trendline to the measured results (solid lines). The impedance was measured within the frequency range of 10 mHz to 1 MHz. (Inset) Equivalent electrical circuit including two series of capacitance/resistance sets corresponding to the grain (G) and grain boundary (GB) effects.

and microstructure of the solid, the higher sintering temperature can provide a denser microstructure with better connectivity and less porosity, thereby improving the dielectric properties.[43]

Complex impedance measurements of the samples were carried out in the frequency range of 10 mHz to 1 MHz, which are depicted as a Nyquist plot in Fig. 5b. The obtained resistivity values are around 560, 720, and 1410 kΩ for the samples sintered at 723, 823, and 923 K, respectively. For all three samples, the semicircular curves display different maximum values of the imaginary part of the impedance, Z'', and intercepts with the real part axis of the impedance, Z'. The values for the pellet sintered at 723 K clearly shows two distinguished semicircular arcs including a small arc at high frequencies (lower region in the Z' axis) and a large arc at low frequencies (higher region in the Z' axis). These two distinctions can be attributed to the contributions of the grains and the grain boundaries, respectively. In polycrystalline materials, the electrical properties can be investigated by discriminating between both grains and grain boundaries with their different structural characteristics. Regarding the defective nature of the grain boundaries causing a scattering of the charge carriers, they can in most cases lead to an increased resistivity.[44] In ceramics, the effects of grain boundaries are commonly interpreted according to the brick layer model.[45] However, in most cases they are more complicated and need to be individually studied and modelled for each case. When **1** is sintered at 723 K, the grain size is comparably small and the ratio of grain boundaries to grains is larger than that of the samples sintered at higher temperatures. Thus, the contribution of the grain boundaries to the impedance values, *i.e.*, both Z'' and Z', is considerably larger than the contribution of the grains.[46] In samples sintered at higher temperatures, the impedance plots present semicircular arcs with two small indents around a Z' of 580 and 300 kΩ for the samples sintered at 823 and 923 K, respectively.

Optical and electrical band structures

According to the results of UV-visible spectroscopy and the derived Tauc plot (Fig. S4†) **1** depicts an indirect optical band gap of 2.00 eV. Attempts to verify the band gap and analysis of the electronic structure by means of quantum chemical calculations, including the calculated partial elemental density of states, PDOS, and total density of states, TDOS, yielded the dominant contribution of the iron ions. The quantum chemical calculations predict an asymmetric band structure for the spin-up and -down contributions (Fig. S5†). However, the band gap is severely underestimated likely due to strong electron correlation that is inadequately entailed in most generalized gradient approximation (GGA) functionals.[47,48] For the quantum chemical calculations, different values of an on-site Coulomb interaction parameter (U) were applied to Fe and the resulting band gap compared to the experimental value from optical spectroscopy. The best value of U, 2.5 eV, was selected to accurately reproduce an indirect band gap of 1.993 eV and a direct band gap of 2.013 eV with a net magnetization of 4.0 μB (3.709×10^{-23} J T^{-1}).

Together with values from the experimental dielectric measurements, these results confirm the semiconductive properties of **1**. The element-projected band structure and DOS are given in Fig. 6. The bottom of the conduction band is populated by Fe-3d orbitals while hybridized states between Fe-d and S-p orbitals are observed near the valence band maximum.

Fig. 7 shows the orbital-resolved DOS of **1** obtained from DFT+U calculations, indicating the main role of the iron and sulphur ions, particularly Fe-d and S-p orbitals, in both the valence and the conduction bands. The spin- and element-resolved DOS plots (Fig. S6 and S7†) display the hybridizations and spin contributions between Fe-d, S-p, and K-s states.

Experimental

General procedure

Due to the air- and moisture-sensitivity of **1** and some of the starting materials, all steps of the synthesis and measurement

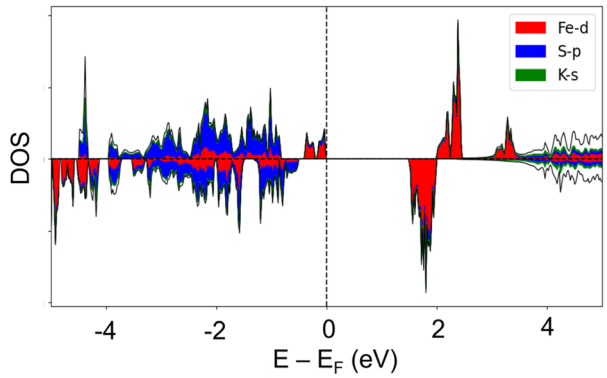

Fig. 6 (a) The element-projected band structure of **1** calculated *via* DFT+U, showing the contribution from potassium (blue), sulphur (green), and iron (red) atoms. Solid lines and dotted lines represent spin-up and spin-down bands respectively. The Fermi level is shifted to zero on the energy scale. (b) The density of states of **1**.

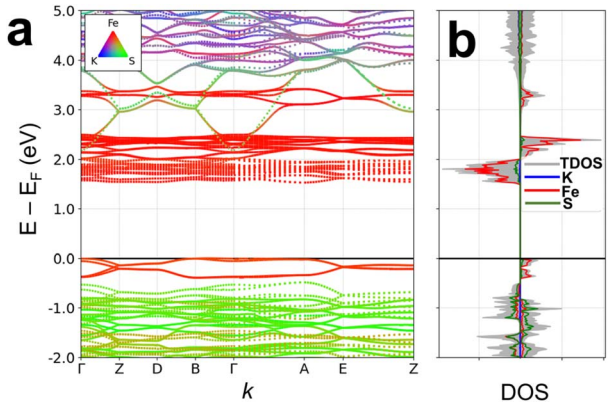

Fig. 7 The orbital-resolved density of states of **1** obtained from DFT+U calculations.(a) Calculated electronic band structure of **1**. (b) Calculated density of states (DOS) of **1**, including total and elemental-resolved DOS plots.

processes were performed under an argon atmosphere using an argon-filled glovebox and/or Schlenk-lines. All solids were used as received without further purification unless noted otherwise. Ethylenediamine was dried over CaH_2 and freshly distilled prior to use.

Synthetic procedures

Synthesis of K_2S. The synthesis process was carried out using 20 g (0.512 mol, 2 eq., Acros Organics, 98%) potassium and 8.2 g (0.258 mol, 1 eq., abcr, 99%) sulphur in liquid NH_3, according to the reported procedure.[49] *Caution: the reaction of sulphur and potassium is exothermic! Cooling and a constant pressure release need to be ensured!* Purity of the product was confirmed by powder X-ray diffraction analysis.

Synthesis of 1. K_2S (10 g, 1.5 eq., 0.090 mol), FeS (10.63 g, 0.120 mol, 2 eq., Sigma-Aldrich, 99%), and sulphur (1.45 g, 0.045 mol, 0.5 eq., abcr, 99%) are mixed and placed in a silica glass ampoule. The ampoule is heated to approx. 1200 K with an oxygen–methane hand torch for about 5 minutes and then allowed to cool down to room temperature. The resulting ingot is removed from the ampoule and ground to obtain the product as a dark-green solid with metallic luster (20.8 g, 0.058 mol, 94.2%).

Preparation of single crystals. 150 mg of **1** and 2 mL of ethylenediamine are added into a 10 mL glass vial and sealed. The reaction mixture is heated to 423 K for 48 h and allowed to cool to room temperature. Single crystals for X-ray diffraction analysis were selected manually under a light microscope.

Further investigations

The details of further characterization and properties investigations such as powder X-ray diffraction and Rietveld refinement, single crystal X-ray diffraction, infrared spectroscopy, magnetometry, dielectric and impedance measurements, SEM/EDX, UV-visible spectroscopy, and quantum chemical calculations are provided in the ESI.†

Conclusions

Pure $K_3[Fe_2S_4]$ (**1**) was prepared using a fast, straightforward, and high yield technique without any further steps of purification. The compound indicates soft ferrimagnetic behaviour with a comparably high magnetisation of around 15 and 22 A m^2 kg^{-1} at 300 and 3 K, which lie within the range of well-known ferrite compounds, originating from the mixed valence of Fe^{II}/Fe^{III}. The simultaneous ferrimagnetic properties and high electrical polarisability of **1** could potentially be considered for spintronic applications. Bulk samples of **1** show different dielectric constant values as well as impedance trends depending on the chosen temperature for the sintering process, indicating a significant impact of the microstructure on the electrical properties. Samples sintered at 923 K, exhibit a dielectric constant of around 1750 at 1 kHz at room temperature which is significantly higher than the reference material SiO_2 ($\kappa = 3.9$) and even higher than most of the commercial dielectric materials. These results introduce an eco-friendly candidate with a strong potential for insulating and high-κ dielectric performances. The optical band gap was determined to be 2.00 eV by UV-visible spectroscopy. The quantum chemical calculations reveal an asymmetric band structure with an energy gap of 1.993 and 2.013 eV indirect and direct band gaps, respectively. These values indicate a semiconductive behaviour of **1**. In combination with the non-toxic, highly abundant elemental constituents, **1** represents a promising material for a range of electronic and magnetic applications.

Author contributions

Conceptualization: M. R. G., G. T.; project administration: M. R. G., G. T.; writing initial draft: M. R. G.; formal analysis: M. R. G.; performance and visualisation of DFT calculations: A. S.; investigation *via* EDX and SEM: J. C. V.; investigation of magnetic properties: K. S.; investigation of UV-visible measurements: B. P.; resources for UV-vis measurements: S.

D.; resources for DFT calculations: P. J.; resources for synthesis, impedance and dielectric properties: G. T.; funding acquisition: G. T.; writing, review and editing: G. T.; supervision: G. T., P. J., S. D.

Conflicts of interest

There are no conflicts to declare.

Acknowledgements

We thank the Verband der Chemischen Industrie e.V. for a Liebig scholarship, the Volkswagen Stiftung within the framework of an "Experiment!" funding, the German-American Fulbright Commission for a Fulbright-Cottrell Award. The authors acknowledge the North-German Supercomputing Alliance (HLRN) for providing High-Performance Computing (HPC) resources that have contributed to the research results. Core facility BioSupraMol is acknowledged for X-Ray diffraction time. We thank Friederike Fuß, Clara A. von Randow, Islam Ramadan, Jan-Erik Fuhrmann, and Moritz Liesegang for their supports in UV-visible spectroscopy, proofreading of the manuscript, SC-XRD, DSC/TG, and PXRD measurements, respectively. We thank Dr Karel Prokes and the Quantum Materials Core Lab facilities at Helmholtz-Zentrum Berlin (HZB) for the magnetic measurements. We acknowledge support by the OpenAccess Publication Fund of Freie Universität Berlin.

Notes and references

1 S. Chaudhuri, D. Salas, V. Srihari, E. Welter, I. Karaman and P. A. Bhobe, Half metallicity in Cr substituted Fe_2TiSn, *Sci. Rep.*, 2021, **11**, 524.

2 M. Ram, A. Saxena, A. E. Aly and A. Shankar, Half-metallicity in new Heusler alloys Mn_2ScZ (Z = Si, Ge, Sn), *RSC Adv.*, 2020, **10**, 7661–7670.

3 X. Wang, M. Lin, X. Shen, Z. Liu, Z. Hu, K. Chen, P. Ohresser, L. Nataf, F. Baudelet, H. J. Lin, C. T. Chen, Y. L. Soo, Y. F. Yang, C. Jin and Y. Long, Enhancement of *A*′-site Mn^{3+} spin ordering by *B*-site Mn^{4+} substitution in quadruple perovskite $PbMn_3Cr_3MnO_{12}$, *Inorg. Chem.*, 2019, **58**(1), 320–326.

4 I. Galanakis, P. H. Dederichs and N. Papanikolaou, Slater-Pauling behavior and origin of the half-metallicity of the full Heusler alloys, *Phys. Rev. B: Condens. Matter Mater. Phys.*, 2002, **66**, 174429.

5 I. Galanakis and P. Mavropoulos, Zinc-blende compounds of transition elements with N, P, As, Sb, S, Se, and Te as half-metallic systems, *Phys. Rev. B: Condens. Matter Mater. Phys.*, 2003, **67**, 104417.

6 D. K. Samarakoon and X. Q. Wang, Intrinsic half-metallicity in hydrogenated boron-nitride nanoribbons, *Appl. Phys. Lett.*, 2012, **100**, 103107.

7 S. Gallego, J. I. Beltran, J. Cerda and M. C. Munoz, Magnetism and half-metallicity at the O surfaces of ceramic oxides, *J. Phys.: Condens. Matter*, 2005, **17**, L451–L457.

8 L. Allf, Magnetic ceramics, 495-510, in *Ceramics Science and Technology*, ed. R. Riedel and I. W. Chen, Wiley-VCH Publication, 2013.

9 Q. U. Ain, S. Naseem and S. Nazir, Robust half-metallicity and magnetic phase transition in Sr_2CrReO_6 via strain engineering, *Sci. Rep.*, 2020, **10**, 13778.

10 F. Giustino, J. H. Lee, F. Trier, M. Bibes, S. M. Winter, R. Valenti, Y. W. Son, L. Taillefer, C. Heil, A. J. Figueroa, B. Placais, Q. S. Wu, O. V. Yazyev, E. P. A. M. Bakkers and J. Nygard, The 2021 quantum materials roadmap, *J. Phys.: Mater.*, 2020, **3**, 042006.

11 Y. Slimani, E. Hannachi, A. Ekicibil, M. A. Almessiere and F. Ben Azzouz, *J. Alloys Compd.*, 2019, **781**, 664–673.

12 M. A. Almessiere, Y. Slimani, H. S. El Sayed, A. Baykal and I. Ercan, *J. Magn. Magn. Mater.*, 2019, **471**, 124–132.

13 Y. Slimani, B. Unal, M. A. Almessiere, E. Hannachi, G. Yasin, A. Baykal and I. Ercan, *J. Mater. Sci.: Mater. Electron.*, 2020, **31**, 7786–7797.

14 N. A. Spaldin and R. Ramesh, Advances in magnetoelectric multiferroics, *Nat. Mater.*, 2019, **18**, 203–212.

15 N. Samarth, Quantum materials discovery from a synthesis perspective, *Nat. Mater.*, 2017, **16**, 1068.

16 Q. Nouailhetas, A. Koblischka-Veneva, M. R. Koblischka, P. K. Naik S., F. Schäfer, H. Ogino, C. Motz, K. Berger, B. Douine, Y. Slimani and E. Hannachi, *AIP Adv.*, 2021, **11**, 015230.

17 M. R. Kolischka, Y. Slimani, A. Koblischka-Veneva, T. Karwoth, X. Zeng, E. Hannachi and M. Murakami, *Materials*, 2020, **13**, 5018.

18 A. K. Pant and E. D. Stevens, Experimental electron-density-distribution study of potassium iron disulfide, a low dimensional material, *Phys. Rev. B: Condens. Matter Mater. Phys.*, 1988, **37**, 1109.

19 I. Han, Z. Jiang, C. dela Cruz, H. Zhang, H. Sheng, A. Bhutani, D. J. Miller and D. P. Shoemaker, Accessing magnetic chalcogenides with solvothermal synthesis: $KFeS_2$ and KFe_2S_3, *J. Solid State Chem.*, 2018, **260**, 1–6.

20 M. Schwarz and C. Röhr, $Cs_8[Fe_4S_{10}]$ and $Cs_7[Fe_4S_8]$, two new sulfido ferrates with different tetrameric anions, *Inorg. Chem.*, 2015, **54**(3), 1038–1048.

21 P. Stüble, S. Peschke, D. Johrendt and C. Röhr, $Na_7[Fe_2S_6]$, $Na_2[FeS_2]$ and $Na_2[FeSe_2]$: new reduced sodium chalcogenido ferrates, *J. Solid State Chem.*, 2018, **258**, 416–430.

22 M. Schwarz, M. Haas and C. Röhr, The Novel alkali sulfidoferrates $K_9[Fe^{III}S_4](S_2)S$, $(K/Rb)_6[Fe^{III}{}_2S_6]$, $Rb_8[Fe^{III}{}_4S_{10}]$, and $K_7[Fe^{II/III}S_2]_s$, *Z. Anorg. Allg. Chem.*, 2013, **639**(2), 360–374.

23 W. Bronger, U. Ruschewitz and P. Müller, New ternary iron sulphides $A_3Fe_2S_4$ (A = K, Rb, Cs): syntheses and crystal structures, *J. Alloys Compd.*, 1995, **218**, 22–27.

24 K. Klepp and H. Boller, $Na_3Fe_2S_4$, ein Thioferrat mit gemischt valenter $^1_\infty[FeS_2]$-Kette, *Monatsh. Chem.*, 1981, **112**, 83–89.

25 K. O. Klepp and W. Sparlinek, Solid state ion exchange chemistry of the solid solution $K_xRb_{1-x}FeS_2$, *Zeitschrift für Kristallographie – Crystalline Materials*, 1996, **211**(9), 626.
26 W. Bronger, H. S. Genin and P. Müller, K_3FeSe_3 und $K_3Fe_2Se_4$, zwei neue Verbindungen im System K/Fe/Se, *Z. Anorg. Allg. Chem.*, 1999, **625**(21), 1462–1473.
27 P. Stüble and C. Röhr, $Cs[FeSe_2]$, $Cs_3[FeSe_2]_2$, and $Cs_7[Fe_4Se_8]$: Missing Links of Known Chalcogenido Ferrate Series, *Z. Anorg. Allg. Chem.*, 2017, **643**(2), 274–278.
28 Y. Guo, H. Wang, Y. Xiao, S. Vogt, R. K. Thauer, S. Shima, P. I. Volkers, T. B. Rauchfuss, V. Pelmenschikov and D. A. Case, Characterization of the Fe site in iron–sulfur cluster-free hydrogenase (Hmd) and of a model compound via nuclear resonance vibrational spectroscopy (NRVS), *Inorg. Chem.*, 2008, **47**, 3969–3977.
29 J. Ensling, P. Gütlich, H. Spiering and K. Klepp, Mössbauer and magnetic studies of mixed-valence linear chain compounds: $Na_3Fe_2S_4$ and $Na_3Fe_2Se_4$, *Hyperfine Interact.*, 1986, **28**, 599–601.
30 W. Bronger and U. Ruschewitz, New ternary iron chalcogenides $A_9Fe_2X_7$ (A = K, Rb, Cs; X = S, Se): synthesis, crystal structure and magnetic properties, *J. Alloys Compd.*, 1993, **197**, 83–86.
31 A. Živković, H. E. King, M. Wolthers and N. H. de Leeuw, Magnetic structure and exchange interactions in pyrrhotite end member minerals: hexagonal FeS and monoclinic Fe_7S_8, *J. Phys.: Condens. Matter*, 2021, **33**, 465801.
32 J. L. Ortiz-Quinonez, U. Pal and M. S. Villanueva, Structural, Magnetic, and Catalytic Evaluation of Spinel Co, Ni, and Co–Ni Ferrite Nanoparticles Fabricated by Low-Temperature Solution Combustion Process, *ACS Omega*, 2018, **3**(11), 14986–15001.
33 S. Debnath and R. Das, Cobalt doping on nickel ferrite nanocrystals enhances the micro-structural and magnetic properties: shows a correlation between them, *J. Alloys Compd.*, 2021, **852**, 156884.
34 S. Bahtiar, A. Taufiq, Sunaryono, A. Hidayat, M. Diantoro, N. Mufti and Mujamilah, Synthesis, investigation on structural and magnetic behaviors of spinel M-ferrite [M = Fe; Zn; Mn] nanoparticles from iron sand, *IOP Conf. Ser.: Mater. Sci. Eng.*, 2017, **202**, 012052.
35 M. A. Almessiere, Y. A. Slimani, M. Hassan, M. A. Gondal, E. Cevik and A. Baykal, Investigation of hard/soft $CoFe_2O_4$/$NiSc_{0.03}Fe_{1.97}O_4$ nanocomposite for energy storage applications, *Int. J. Energy Res.*, 2021, **45**, 16691–16708.
36 M. B. Taj, M. D. F. Alkahtani, A. Raheel, S. Shabbir, R. Fatima, S. Aroob, R. Yahya, W. Alelwani, N. Alahmadi, M. Abualnaja, S. Noor, R. H. Ahmad and H. Alshater, Bioconjugate synthesis, phytochemical analysis, and optical activity of $NiFe_2O_4$ nanoparticles for the removal of ciprofloxacin and Congo red from water, *Sci. Rep.*, 2021, **11**, 5439.
37 J. K. Rajput and G. Kaur, Synthesis and applications of $CoFe_2O_4$ nanoparticles for multicomponent reactions, *Catal. Sci. Technol.*, 2014, **4**, 142–151.
38 F. Shams, M. R. Ghazanfari and C. Schmitz-Antoniak, Magnetic-Plasmonic Heterodimer Nanoparticles: Designing Contemporarily Features for Emerging Biomedical Diagnosis and Treatments, *Nanomaterials*, 2019, **9**, 97.
39 H. Liu, D. Liang and S. Chen, Evolution of magnetic and transport properties in pyrochlore iridates $A_2Ir_2O_7$ (A=Y, Eu, Bi), *Wuhan Univ. J. Nat. Sci.*, 2017, **22**, 215.
40 K. H. Fischer and J. A. Hertz, *Spin Glasses*, Cambridge Studies in Magnetism, Cambridge University Press, 1993, vol. 1.
41 G. D. Wilk, R. M. Wallace and J. M. Anthony, High-κ gate dielectrics: current status and materials properties considerations, *J. Appl. Phys.*, 2001, **89**, 5243.
42 W. B. Li, D. Zhou, L. X. Pang, R. Xu and H. H. Guo, *J. Mater. Chem. A*, 2017, **37**, 19607.
43 J. Qi, M. Cao, Y. Chen, Y. Fang, W. Pan, H. Hao, Z. Yao, Z. Yu and H. Liu, Effects of sintering temperature on microstructure and dielectric properties of $Sr_{0.985}Ce_{0.01}TiO_3$ ceramics, *J. Alloys Compd.*, 2018, **762**, 950–956.
44 H. Bishara, S. Lee, T. Brink, M. Ghidelli and G. Dehm, Understanding grain boundary electrical resistivity in Cu: the effect of boundary structure, *ACS Nano*, 2021, **15**, 16607–16615.
45 S. Nazir, Insulator-to-half metal transition and enhancement of structural distortions in Lu_2NiIrO_6 double perovskite oxide via hole-doping, *Sci. Rep.*, 2021, **11**, 1240.
46 D. Huang, W. L. Li, Z. F. Liu, Y. X. Li, C. Ton-That, J. Cheng, W. C. H. Choy and F. C. C. Ling, Electron-pinned defect dipoles in (Li, Al) co-doped ZnO ceramics with colossal dielectric permittivity, *J. Mater. Chem. A*, 2020, **8**, 4764.
47 H. j. Kulik, Perspective: treating electron over-delocalization with the DFT+U method, *J. Chem. Phys.*, 2015, **142**, 240901.
48 J. Zhang, Y. Li and J. Chen, Water-oxygen interaction on marcasite (1 0 1) surface: DFT calculation, *Int. J. Min. Sci. Technol.*, 2022, **32**, 191.
49 M. R. Ghazanfari, A. Santhosh, K. Siemensmeyer, F. Fuß, L. Staab, J. C. Vrijmoed, B. Peters, M. Liesegang, S. Dehnen and O. Oeckler, Large exchange bias, high dielectric constant, and outstanding ionic conductivity in single-phase spin glass, *Adv. Electron. Mater.*, 2022, 2200483.